

Polarizable Density Embedding: A New QM/QM/MM-Based Computational Strategy

Jógvan Magnus Haugaard Olsen,^{*,†,‡} Casper Steinmann,[‡] Kenneth Ruud,[§] and Jacob Kongsted^{*,‡}

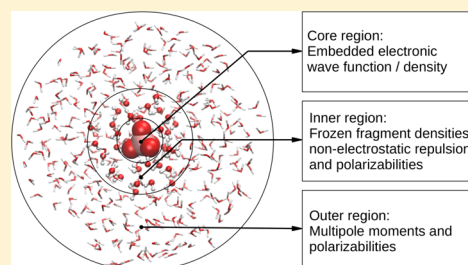
[†]Laboratory of Computational Chemistry and Biochemistry, Ecole Polytechnique Fédérale de Lausanne, CH-1015 Lausanne, Switzerland

[‡]Department of Physics, Chemistry and Pharmacy, University of Southern Denmark, DK-5230 Odense M, Denmark

[§]Centre for Theoretical and Computational Chemistry, Department of Chemistry, University of Tromsø—The Arctic University of Norway, N-9037 Tromsø, Norway

S Supporting Information

ABSTRACT: We present a new QM/QM/MM-based model for calculating molecular properties and excited states of solute–solvent systems. We denote this new approach the polarizable density embedding (PDE) model, and it represents an extension of our previously developed polarizable embedding (PE) strategy. The PDE model is a focused computational approach in which a core region of the system studied is represented by a quantum-chemical method, whereas the environment is divided into two other regions: an inner and an outer region. Molecules belonging to the inner region are described by their exact densities, whereas molecules in the outer region are treated using a multipole expansion. In addition, all molecules in the environment are assigned distributed polarizabilities in order to account for induction effects. The joint effects of the inner and outer regions on the quantum-mechanical core part of the system is formulated using an embedding potential. The PDE model is illustrated for a set of dimers (interaction energy calculations) as well as for the calculation of electronic excitation energies, showing promising results.



INTRODUCTION

The formulation and benchmarking of quantum chemically based models for solvation has for a long time been an active area of research.^{1,2} This interest has arisen as a consequence of the fact that most chemistry takes place in some kind of liquid or solid-state environment. The significant increase in complexity when going from the gas phase to a solution in general prohibits the use of accurate conventional quantum-chemical methods for describing the effects of the solvent. In fact, brute-force use of any quantum-chemical method to the entire solute–solvent system would in many cases not be computationally efficient because in most cases the interest is not in a detailed electronic structure description of the solvent but rather the solute. Focused methods are much more effective in the sense that only the electronic structure of the solute is considered in detail and at a high level of accuracy.

Dielectric continuum models belong to the class of focused solvation models. One of the most advanced quantum chemically based dielectric continuum models is the polarizable continuum model (PCM) originally formulated by Tomasi and co-workers.^{1,3–5} The PCM has over the years shown its versatility for modeling a wide range of chemical and physical properties as well as chemical reactions of molecular systems, and the PCM has led to significant insight into many chemical problems associated with different aspects of solvation.

Even though new developments of the PCM continue to be an active field of research,¹ solvation models that keep an

atomistic reference to the environment are becoming increasingly popular. Discrete solvation models have the advantage of providing a more realistic description of the environment and can in fact be applied more broadly than the PCM. For instance, discrete models can also be used to model environmental effects due to a structured environment such as a protein. The most common of such discrete models is the quantum mechanical–molecular mechanical^{6–8} (QM/MM) model which has been developed in several variants that differ in their complexity. The electrostatic embedding QM/MM^{9–12} scheme includes interactions that polarize the quantum region, whereas the polarized embedding QM/MM scheme includes a polarizable environment.^{13–20} The discrete and continuum models can also be combined to form a two-layered description of the environment.^{21–24}

We have in recent years been developing a polarizable embedding (PE) model,^{25–31} which is a QM/MM-type computational scheme where an embedded, focused part of the total system is described at the flexible and accurate level of quantum mechanics, whereas the surroundings are described by a classical mechanics model. In this model, different kinds of

Special Issue: Jacopo Tomasi Festschrift

Received: October 7, 2014

Revised: January 10, 2015

Published: January 16, 2015



environments can be treated on the same footing, for instance solvents and structured environments such as a protein matrix. Although the PE model shares some similarities with conventional QM/MM methods, it is more advanced in that it (i) derives the parameters defining the environment (i.e., the embedding potential) based on quantum-mechanical calculations; (ii) it includes an explicit polarization of the environment that is also included in the embedding potential, and (iii) it has been extended to quantum-mechanical response theory^{32,33} and is thereby designed for the calculation of excited states and general response properties such as electrical and magnetic molecular properties.

In the PE model, the charge distribution defining the molecules in the environment is obtained by performing a multicenter multipole expansion, giving rise to distributed charges, dipoles, quadrupoles, etc. in the environment. The expansion centers are usually taken to be the position of the atomic nuclei of the molecules in the environment. The use of a multipole expansion is computationally advantageous because all interaction terms between the quantum-mechanically described core and the environment parts of the total system can be calculated based on one-electron contributions. However, as the distance between the quantum and classical parts is reduced, the use of this multipole description may not be accurate enough.^{25,34} In addition to describing the environment by permanent multipoles, the PE model also assigns an anisotropic polarizability to each expansion center in the environment. Such polarizabilities will, following the classical expressions, give rise to induced dipole moments and thereby an induced charge distribution. The PE model is fully self-consistent in the sense that both the quantum-mechanical and classical equations describing the polarization (or, more precisely, orbital rotations in the quantum subsystem) are solved self-consistently.²⁶

Here we extend the embedding potential underlying the PE model in two different directions. First, we explore the use of nonmultipole-expanded densities defining the molecules in the environment. This increases the computational cost of the model since now also the intermolecular part of the two-electron Coulomb integral matrix between the quantum system and each molecule in the environment is needed. However, the use of exact densities instead of the multipole expansion allows for a more physically correct description of the interaction between the solute and the solvent since there are no inaccuracies caused by a multipole-expanded potential. Second, we include in the embedding potential a component representing nonelectrostatic repulsion based on a projection operator originally proposed by Huzinaga and Cantu.³⁵ The nonelectrostatic repulsion (sometimes referred to as exchange- or Pauli-repulsion) is introduced in terms of orbital overlap between the quantum and classical subsystems. We name this new model polarizable density embedding (PDE). It has some similarities to other QM/QM-based methods such as the fragment molecular orbital^{36,37} (FMO), frozen density embedding^{38–42} (FDE), Gaussian electrostatic model^{43,44} (GEM), and fragment embedding ab initio model potential^{45,46} (FAIMP) methods. The most common aspect of these methods is the treatment of Coulomb interactions using a continuous electron density. However, in contrast to other methods, the environment in PDE contains an explicit account of polarization effects through the use of the aforementioned polarizability model. Thus, the PDE method is effective in modeling the induced charge distribution (polarization) of the

environment and thereby avoids the costly iterative schemes needed in order to relax the environment (e.g., the freeze-and-thaw cycles in FDE).³⁹ Furthermore, based on the current PE implementation, it is straightforward to implement the PDE model within a quantum-mechanical response theory formulation, thus giving access to excited states and, more generally, to molecular properties. This allows us to take advantage of the efficiency and simplicity of the polarizability model to include differential polarization effects, which can otherwise be complicated and expensive to incorporate in standard QM/QM-type embedding schemes.^{41,42,47} The FAIMP method also uses the projection operator to model nonelectrostatic repulsion which, due to the iterative scheme used, is included between all molecules/fragments. FDE includes nonelectrostatic repulsion using the so-called non-additive kinetic energy functional. The PDE model is a focused approach where only a part of the total system is treated at a higher level. Thus, the nonelectrostatic repulsion enforces orthogonality between molecules in the core part and relevant molecules in the environment but not between the molecules within the environment.

THEORY

In this section, we present the equations that define the proposed extensions to the PE model, formulated in an atomic orbital (AO)-based self-consistent field (SCF) formalism. We refer to refs 26 and 48 for a detailed description of the basic PE model.

In the following, we will consider molecular systems that can be separated into noncovalently bound fragments. Furthermore, the total system is divided into three subsystems: a core region, an inner region, and an outer region. The fragments are distributed into the respective regions according to their expected importance. The central fragments constitute the core, which is the part of the system that we want to optimize using quantum methods in the presence of all other fragments. The fragments closest in space to the core define the inner region, and all the remaining fragments define the outer region. The permanent charge distribution of fragments belonging to the inner region are represented by quantum-mechanically calculated densities, whereas fragments in the outer region are described by atom-centered multipole moments. The induced charge distribution in each fragment (caused by the electric field from the other fragments) in both the inner and outer regions is described by induced dipole moments obtained from (distributed) anisotropic polarizabilities. In addition, we add a repulsive potential to each fragment in the inner region in order to include nonelectrostatic repulsion effects. The combined inner and outer regions comprise an embedding potential. Note that the polarization of the core is included through the optimization of the wave function/density in the presence of the embedding potential.

The effects of the environment are incorporated in the SCF equations through an effective operator

$$\hat{f}^{\text{eff}} = \hat{f}^{\text{vac}} + \hat{v}^{\text{PDE}} \quad (1)$$

where \hat{f}^{vac} is the usual vacuum Fock or Kohn–Sham (KS) operator, and \hat{v}^{PDE} is an embedding potential operator that describes the interactions with the environment. The PDE operator consists of several contributions

$$\hat{v}^{\text{PDE}} = \hat{v}^{\text{es}} + \hat{v}^{\text{ind}} + \hat{v}^{\text{rep}} \quad (2)$$

that each represents different intermolecular interactions. The \hat{v}^{es} operator describes electrostatic interactions, \hat{v}^{ind} is an induction operator that includes the polarization of the environment, and \hat{v}^{rep} models the effects of nonelectrostatic repulsion. In the following, we will provide detailed expressions for each operator separately, focusing on the new terms added compared to the basic PE model. Furthermore, we will only consider interactions with the electrons in the core, noting that there is also an energy contribution from the interactions with the nuclei in the core.

We start with the electrostatic operator, that we will further separate into two contributions

$$\hat{v}^{\text{es}} = \hat{v}^{\text{mul}} + \hat{v}^{\text{fd}} \quad (3)$$

where the \hat{v}^{mul} operator describes the interactions between electrons in the core region and the multipole moments in the outer region. Details concerning this operator are found in refs 25, 26, and 48. The \hat{v}^{fd} operator contains the electrostatic interactions between the electrons in the core region and the fragment densities in the inner region. An AO Fock/KS matrix element of the \hat{v}^{fd} operator is given by

$$v_{\mu\nu}^{\text{fd}} = \sum_{a=1}^{N_{\text{in}}} \left(- \sum_{m \in a}^{M_a} Z_m v_{\mu\nu}(\mathbf{R}_m) + \sum_{\gamma\delta \in a} D_{\gamma\delta} v_{\mu\nu,\gamma\delta} \right) \quad (4)$$

Equation 4 defines the electrostatic interactions between electrons in the core, and nuclei and electrons in the inner region. We sum over N_{in} fragments in the inner region, and accordingly, Z_m is the m th nucleus of the M_a nuclei in the a th fragment, and $v_{\mu\nu}(\mathbf{R}_m)$ is a one-electron potential energy integral defined as

$$v_{\mu\nu}(\mathbf{R}_m) = \int \frac{\chi_{\mu}(\mathbf{r})\chi_{\nu}(\mathbf{r})}{|\mathbf{R}_m - \mathbf{r}|} d\mathbf{r} \quad (5)$$

where χ_{μ} and χ_{ν} are AO basis functions belonging to the core region and \mathbf{R}_m is the position of the m th nucleus. The last term in eq 4 contains the AO density matrix of a fragment in the inner region and the intermolecular two-electron integrals that are given by

$$v_{\mu\nu,\gamma\delta} = \iint \frac{\chi_{\mu}(\mathbf{r})\chi_{\nu}(\mathbf{r})\chi_{\gamma}(\mathbf{r}')\chi_{\delta}(\mathbf{r}')}{|\mathbf{r} - \mathbf{r}'|} d\mathbf{r} d\mathbf{r}' \quad (6)$$

where the orbital indices are separated with a comma to indicate that μ and ν always belong to the core region and γ and δ belong to a fragment in the inner region.

The second term in the PDE operator (eq 2) is the induction part describing the polarization of the fragments in both the inner and outer region through the use of classical polarizabilities. In general, it involves multipole expansions yielding dipole–dipole, dipole–quadrupole, quadrupole–quadrupole polarizabilities, and so on. Furthermore, nonlinear polarization can be included using hyperpolarizabilities. Here we will only use anisotropic dipole–dipole polarizabilities. This operator has been described in detail before (see, for example, refs 25, 26, and 48). However, since it is a key component of the extended embedding model proposed here, we will provide some details of this operator. The Fock/KS matrix elements are of the form

$$v_{\mu\nu}^{\text{ind}} = - \sum_{a=1}^{N_{\text{tot}}} \sum_{s \in a}^{S_a} \sum_{\alpha}^{x,y,z} \mu_{\alpha,s}^{\text{ind}} t_{\alpha,\mu\nu}(\mathbf{R}_s) \quad (7)$$

where we now sum over all fragments in both the inner and outer regions and all polarizable sites within each fragment. This matrix element contains induced dipole moments, μ_s^{ind} , located at the polarizable site s in the given fragment, and electric-field integrals

$$t_{\alpha,\mu\nu}(\mathbf{R}_s) = - \int \chi_{\mu}(\mathbf{r}) \frac{(R_{\alpha,s} - r_{\alpha})}{|\mathbf{R}_s - \mathbf{r}|^3} \chi_{\nu}(\mathbf{r}) d\mathbf{r} \quad (8)$$

The induced dipole moments are determined by the total electric field exerted on the polarizable site

$$\mu_s^{\text{ind}} = \alpha_s [\mathbf{F}_{\text{mul}}(\mathbf{R}_s) + \mathbf{F}_{\text{fd}}(\mathbf{R}_s) + \mathbf{F}_{\text{core}}(\mathbf{R}_s) + \mathbf{F}_{\text{ind}}(\mathbf{R}_s)] \quad (9)$$

where α_s is a polarizability tensor and the electric fields come from the multipole moments in the outer region, $\mathbf{F}_{\text{mul}}(\mathbf{R}_s)$, the fragment densities in the inner region, $\mathbf{F}_{\text{fd}}(\mathbf{R}_s)$, the quantum core, $\mathbf{F}_{\text{core}}(\mathbf{R}_s)$, and the other induced dipole moments, $\mathbf{F}_{\text{ind}}(\mathbf{R}_s)$, respectively. The polarizabilities are obtained from a quantum-mechanical calculation of the isolated fragments and are typically distributed to the atomic sites of a given fragment. Note that eq 9 has to be solved self-consistently because the last field contribution depends on the induced dipoles. The electric fields from the multipole moments and fragment densities are static throughout an embedding calculation. However, since the electric field from the core depends on the wave function/density, we update the induced dipole moments in each SCF cycle. Furthermore, we determine the induced dipole moments self-consistently in the field from all the other induced dipole moments. We note that in a perturbation expansion of intermolecular interaction energies, this corresponds to inclusion of some polarization effects to infinite order.⁴⁹

The last part of the PDE operator (eq 2) models short-range, nonelectrostatic repulsion effects (often referred to as exchange- or Pauli-repulsion), which otherwise are included only as energies in classical embedding schemes such as QM/MM. Including only electrostatic (and polarization) interactions corresponds to a nonoverlapping fragment–fragment wave function approximation. This approximation can introduce large errors at short intermolecular distances where there can be significant wave function overlap.^{50,51} Such errors can, to some extent, be corrected by adding energy corrections, but this will not affect the electronic properties of the embedded core. In the PDE model, we use the projection operator method by Huzinaga and Cantu³⁵ to enforce orthogonality between the core and inner-region fragments. The Fock/KS matrix elements of this operator are given by

$$v_{\mu\nu}^{\text{rep}} = - \sum_{a=1}^{N_{\text{in}}} \sum_{\gamma\delta \in a} W_{\gamma\delta} S_{\mu\gamma} S_{\nu\delta} \quad (10)$$

in an AO basis. The $S_{\mu\gamma}$ and $S_{\nu\delta}$ elements are intermolecular overlap integrals, and $W_{\gamma\delta}$ is an element of an energy-weighted density matrix defined as

$$W_{\gamma\delta} = \sum_{i=1}^{N_{\text{occ}}} \epsilon_i C_{\gamma i} C_{\delta i} \quad (11)$$

Here we sum over the occupied molecular orbitals (MOs) of the inner-region fragments. Thus, ϵ_i is an MO energy and $C_{\gamma i}$ and $C_{\delta i}$ are MO coefficients. These are calculated for each fragment in isolation.

We now briefly introduce the PDE formalism within quantum-mechanical response theory.^{32,33} The PDE model does not introduce new wave function/density dependencies compared to the basic PE model. We will therefore just give a brief overview of the approach and limit ourselves to the case of linear response.

To obtain the time-dependent orbital-rotation response parameters, we solve the linear response equation

$$(\mathbf{E}^{[2]} - \omega \mathbf{S}^{[2]}) \mathbf{\kappa}^\omega = \mathbf{V}^{[1]} \quad (12)$$

where $\mathbf{\kappa}^\omega$ is a response vector containing the first-order response parameters, $\mathbf{E}^{[2]}$ is the electronic Hessian, $\mathbf{S}^{[2]}$ the metric, sometimes also referred to as the generalized overlap matrix, and $\mathbf{V}^{[1]}$ is the property gradient. For transition properties (i.e., excitation energies), an equation similar to eq 12 is solved but with the right-hand side set to zero; that is, a generalized eigenvalue equation. The PDE contributions only appear in the electronic Hessian, and it should be noted that we have an explicit density dependence through the electric field as shown in eq 9. The PDE contributions to the electronic Hessian can be written as

$$\mathbf{E}_{\text{PDE}}^{[2]} = \langle 0 | [\hat{q}, [\hat{\rho}^{\text{PDE}}, \hat{q}^\dagger]] | 0 \rangle + \langle 0 | [\hat{q}, \hat{\rho}^{\text{ind}}(\omega)] | 0 \rangle \quad (13)$$

where $|0\rangle$ represents the reference state and \hat{q} is an orbital rotation operator.³² The last term in this equation yields the response of the environment due to the applied perturbation, and this term is often named the dynamical response. When considering transition properties, this last term accounts for differential polarization effects arising from a transition from the reference state to the excited state. Using an AO formulation, we write this contribution as

$$v_{\mu\nu}^{\text{ind}}(\omega) = - \sum_{a=1}^{N_{\text{tot}}} \sum_{s \in a} \sum_{\alpha}^{x,y,z} \mu_{\alpha,s}^{\text{ind}}(\omega) t_{\alpha,\mu\nu}(\mathbf{R}_s) \quad (14)$$

where the induced dipole moments, $\mu_s^{\text{ind}}(\omega)$, are obtained as

$$\mu_s^{\text{ind}}(\omega) = \alpha_s [\mathbf{F}_{\text{core}}^\omega(\mathbf{R}_s) + \mathbf{F}_{\text{ind}}^\omega(\mathbf{R}_s)] \quad (15)$$

The elements of the perturbed electric field from the core electrons, $\mathbf{F}_{\text{core}}^\omega(\mathbf{R}_s)$, are given by

$$\mathbf{F}_{\alpha,\text{core}}^\omega(\mathbf{R}_s) = - \sum_{\mu\nu} t_{\alpha,\mu\nu}(\mathbf{R}_s) D_{\mu\nu}^\omega \quad (16)$$

where the $t_{\alpha,\mu\nu}(\mathbf{R}_s)$ integral is defined in eq 8 and $D_{\mu\nu}^\omega$ is an element of the first-order perturbed density matrix (the transition density matrix)

$$D_{\mu\nu}^\omega = \sum_{ia} \kappa_{ia}^\omega C_{\mu i} C_{\nu a} \quad (17)$$

The induced dipole moments are again determined self-consistently in the field of all the other induced dipole moments and describe the response of the environment due to the first-order differential polarization between the ground and excited states.

COMPUTATIONAL STRATEGY

The workflow of a PDE calculation can be described as follows. Starting from a molecular structure, we (1) identify fragments belonging to the core, inner, and outer regions based on geometrical criteria; (2) calculate distributed multipole moments and distributed polarizabilities for each fragment in the outer region; (3) calculate the density matrix, MO energies,

MO coefficients, the electric field at all polarizable sites, and the distributed polarizabilities for each fragment in the inner region; (4) pair each inner-region fragment with the core and calculate intermolecular two-electron and overlap integrals; (5) optimize the wave function/density of the core region in the presence of the embedding potential and calculate the properties of interest.

The workflow in going from structure to property is handled by a Python script that automates and parallelizes the workflow described above and will be released in the near future. Defining each of the five steps above, such as the method and basis set to use for the inner- and outer-region fragments, can be given as input to the script. Furthermore, the distribution of the fragments into the different regions is also given as input.

In the second step, we perform calculations on the outer-region fragments in order to obtain distributed multipole moments and polarizabilities. Here, it is also possible to instead calculate atom-centered point charges that are fitted to reproduce the electrostatic potential or even use standard potentials. The resulting parameters are stored in a potential file that is read in the final calculation on the core region.

The third step involves calculations on the inner-region fragments in order to obtain the fragment density matrices, molecular orbitals, and molecular orbital energies and at the same time the electric field at all polarizable sites. The latter is needed to calculate induced moments in the final embedding calculation. In the last preparatory step, we pair each inner-region fragment with the core and calculate the necessary two-electron and overlap integrals. To increase efficiency, we modified the two-electron integral code in the Dalton program⁵² so that only the relevant intermolecular integrals are calculated. The fragment density matrices, MOs, and MO energies, calculated in the previous steps, are then read and used to form the electrostatic and nonelectrostatic repulsion contributions to the Fock/KS matrix. The fifth and final step is the calculation on the core region, where the quantities from the previous steps are used in the embedding potential.

COMPUTATIONAL DETAILS

The distributed multipole moments, assigned to atomic sites in the outer region, and polarizabilities, assigned to all atomic sites in the inner and outer region, were calculated using the localized properties (LoProp) method by Gagliardi et al.⁵³ as implemented in MOLCAS.⁵⁴ Geometry optimizations and PCM calculations (using default settings) were performed using Gaussian 09.⁵⁵ All other calculations were performed using a development version of the Dalton program.⁵² Contributions related to the PDE and PE models are handled by the PE library⁵⁶ which has been interfaced to Dalton. All one-electron integrals required by the PE library are calculated using the GenInt library of Gao, Thorvaldsen, and Ruud.^{57,58} For these calculations, we made use of the BLYP,^{59–61} B3LYP,^{60,62–64} and CAM-B3LYP⁶⁵ exchange-correlation functionals, the 6-31G and 6-31+G* basis sets,^{66–69} as well as the cc-pVDZ, aug-cc-pVDZ, and aug-cc-pVTZ basis sets.^{70–73}

For the excitation energies, the structures used were taken from molecular dynamics (MD) trajectories in order to take into account the dynamical nature of the solute–solvent systems. The reported values are thus averages based on a number of (uncorrelated) structures. The systems considered are the permanganate ion (MnO_4^-) and *p*-nitroaniline (pNA), both in water solution.

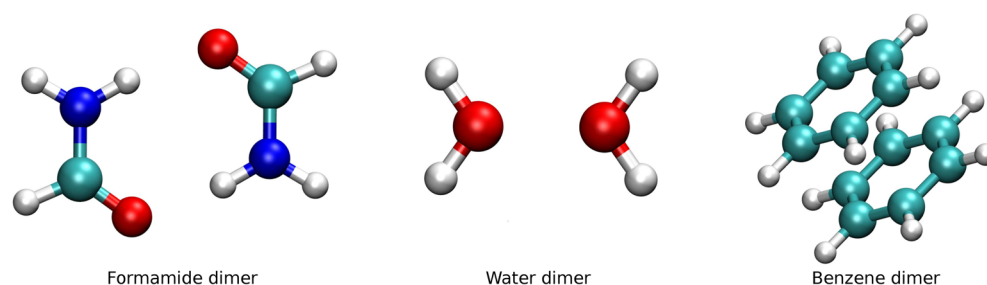


Figure 1. Dimers used in the interaction energy calculations.

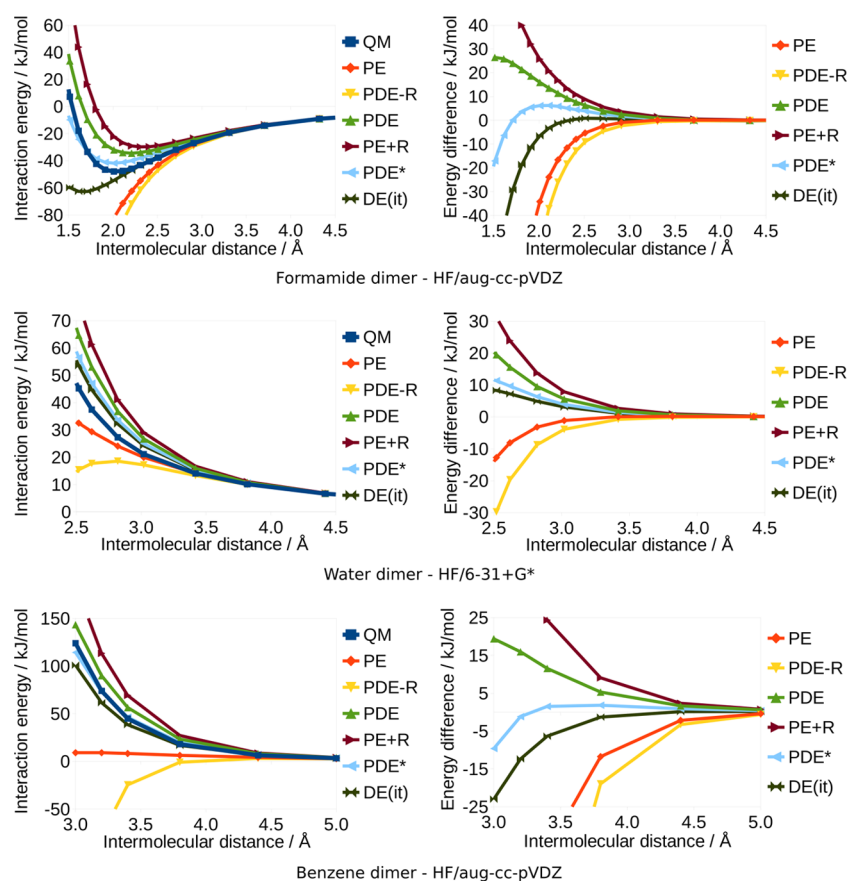


Figure 2. Interaction energy curves and energy differences compared to the QM reference. *Nonelectrostatic repulsion was scaled by a factor of 0.8.

The structures of MnO_4^- in water solution [516 water molecules (approximately 15 Å sphere)] were extracted from ten separate 0.1 ns BLYP/6-31G/TIP3P⁷⁴ MD trajectories. Each trajectory was equilibrated for 0.02 ns before the 0.1 ns production runs. The starting structures for the production runs were extracted from a 0.1 ns BLYP/STO-3G^{75,76}/TIP3P MD simulation. We used ten structures from each 0.1 ns trajectory, adding up to give a total of 100 structures. The structures of MnO_4^- in vacuum were from a single pre-equilibrated 1.0 ns BLYP/6-31G MD trajectory. The QM and QM/MM MD simulations were performed using TeraChem,⁷⁷ where the default time step of 1.0 fs was used. The temperature was set to 300 K controlled by a Langevin thermostat with 200.0 fs damping time. We used spherical boundary conditions to constrain the density to 1.1059 g/mL. Furthermore, a constant 0.01 au force was put on the Mn atom to steer it toward the center of the water cluster.

The pNA structures are based on a rigid body classical MD simulation using a polarizable force field. The trajectory is originally from ref 78, and we refer to that work for more details. We used 120 structures extracted from the trajectory and included water molecules that were within 10 Å from pNA.

RESULTS AND DISCUSSION

We will first benchmark the hybrid quantum-classical embedding potential method by comparing dimer interaction energies to quantum-mechanical reference data. We note that the aim of the PDE (and PE) model is not to accurately reproduce ground-state energies but rather to calculate molecular response properties. After discussing these interaction energies, we present excitation energy calculations of two solute–solvent systems.

Interaction energies. To benchmark the PDE model, we performed interaction energy calculations using three different systems: formamide, water, and benzene dimers. We calculated

the energy at varying intermolecular distances, keeping each molecule rigid and maintaining symmetry. Examples of the structures are shown in Figure 1. Note that the water and benzene dimers are in a purely repulsive conformation.

The reference interaction energies were calculated by subtracting the isolated monomer energies from the dimer energy, correcting for basis set superposition error (BSSE) using the counterpoise (CP) procedure.^{79,80} All other interaction energies were calculated by subtracting the energy of an isolated monomer from the energy of an embedded monomer. Only one molecule is represented by the embedding potential, and for this molecule we use either multipole moments up to quadrupoles or fragment densities to model the permanent charge distribution. The induced charge distribution is always obtained using anisotropic polarizabilities. Although electron correlation effects are important in order to treat weak intermolecular interactions accurately, we use Hartree–Fock (HF) wave functions throughout both for the reference calculations, for the embedded monomer and for the components of the embedding potential in order to simplify the comparisons.

The interaction energy curves and energy differences compared to the references are shown in Figure 2. Here we clearly see the effect of the repulsion operator. The PDE-R energies, which do not include the repulsion operator, diverge as the intermolecular distance is reduced, as one might expect from a purely electrostatic description, whereas including the nonelectrostatic repulsion results in the correct behavior. However, the repulsive effect is increasingly overestimated for shorter distances. In the case of the bonding formamide dimer, we observe relatively small errors around the equilibrium distance (1.8–2.2 Å) although the equilibrium distance is shifted slightly to a longer bond length relative to the QM reference. Interestingly, the interactions present in the basic PE model are “softer” compared to PDE-R, even though both models do not include explicit nonelectrostatic repulsion. This can be explained by the fact that the electronic and nuclear charges are combined to form (small) point charges in the PE case, whereas there in the PDE model are large nuclear point charges and “diffuse” electron clouds. For the same reason, combining the nonelectrostatic repulsion with the classical PE model results in a larger overestimation than PDE (see PE+R in Figure 2).

We also performed calculations where the projection operator is scaled by a factor of 0.8 in order to reduce the repulsive effect (see PDE* in Figure 2). This improves the interaction energies compared to the nonscaled results. However, it leads to an underestimation at very short distances for the formamide and benzene dimers while still slightly overestimating the energies at other distances. Thus, it is not possible to use a simple scaling to achieve exact agreement at all distances. This is consistent with previous findings where overlap-based repulsion potentials were used.^{81,82} Still, the simple scaling is surprisingly good with relatively small errors, even at distances that are highly repulsive, and in the case of the formamide dimer, we find that the equilibrium distance is reproduced quite well.

To investigate more closely the basis set effects, we performed additional calculations on the formamide dimer using different basis sets. The results are shown in Tables 1 and 2 as energy differences compared to the reference interaction energies. The PDE model with nonscaled repulsion (Table 1) produces errors that are between 5–15 kJ/mol around the

Table 1. Basis Set Effects on the Formamide Dimer Interaction Energy Differences

R (Å)	$E_{\text{int}}^{\text{PDE-QM}}$ (kJ/mol)			
	6-31G	6-31G*	6-31+G*	aug-cc-pVDZ
1.8	14.90	15.47	18.28	21.32
1.9	11.68	12.55	15.98	18.61
2.0	9.26	10.11	13.57	15.92
2.1	7.44	8.16	11.32	13.54
2.2	5.96	6.64	9.32	11.40

Table 2. Basis Set Effects on the Formamide Dimer Interaction Energy Differences using Scaled Nonelectrostatic Repulsion

R (Å)	$E_{\text{int}}^{\text{PDE*}-\text{QM}}$ (kJ/mol)			
	6-31G	6-31G*	6-31+G*	aug-cc-pVDZ
1.8	−1.64	−0.92	0.60	3.71
1.9	0.20	1.16	2.75	5.51
2.0	1.40	2.29	3.70	6.17
2.1	2.10	2.84	3.95	6.23
2.2	2.36	3.04	3.82	5.89

*Nonelectrostatic repulsion was scaled by a factor of 0.8.

equilibrium distance (1.8–2.2 Å) when using the smallest basis set and increase to 10–20 kJ/mol for the largest basis set. Using instead the scaled repulsion potential (Table 2) reduces the errors to below 3 kJ/mol for the smallest basis set and below 7 kJ/mol for the largest basis set. Furthermore, we observe that the repulsive effect increases with basis set size, thus leading to larger errors for larger basis sets (depending on whether a scaled repulsion potential is used or not). This effect is most likely connected to the fact that the fragment density is calculated in isolation and therefore extends too far into the core region, i.e., the more flexible the basis set is, the larger the extent of the electron density will be (up to a limit). This will only affect the nonelectrostatic repulsion and not the electrostatic interactions, since the relaxation effects of the latter are modeled using classical polarization. This is consistent with the results obtained using a relaxed embedding potential density (see DE(it) in Figure 2), which is determined by optimizing the density of an embedded monomer and then using this optimized density to optimize the density of the other monomer and repeat until converged densities are obtained. Here we see that the DE(it) reproduce the QM reference quite well but are underestimated at shorter distances, consistent with previous findings.^{81,82} The water dimer is an exception because other effects, such as charge-transfer and exchange interactions, are more important.

Finally, we emphasize that the aim of the PDE model is not to accurately reproduce interaction energies but to calculate response properties. Nevertheless, the results presented in this section show that the PDE model not only has a physically correct behavior but also reproduces interaction energies quite well at distances that are relevant when calculating properties.

Excitation Energies. Permanganate Ion. Our first illustration of the PDE model for excited-state calculations is the permanganate ion, MnO_4^- , solvated in water, where we calculate the solvent shift of the lowest singlet excitation ($1t_1 \rightarrow 2e$). We performed PDE-CAM-B3LYP/cc-pVDZ calculations on 100 structures (MnO_4^- and 516 water molecules) taken from a total of 1.0 ns BLYP/6-31G/TIP3P MD trajectories. Furthermore, in order to extract the solvent shift compared

to gas phase, we also calculated the excitation energies at the CAM-B3LYP/cc-pVDZ level of theory using 100 structures from the 1.0 ns BLYP/6-31G trajectory. The cc-pVDZ basis set was chosen based on a basis set analysis performed on a random snapshot (see Table S1 of the Supporting Information). In addition to the averaging of the 100 structures, we also averaged over the three lowest excitation energies of each structure, since the triply degenerate $1t_1 \rightarrow 2e$ transitions become nondegenerate when the molecule is not in the equilibrium geometry.

To investigate the convergence with respect to the size of the core region, we performed a series of calculations, including an increasing amount of water molecules in the core region. All other water molecules are in the inner region, being represented by fragment densities, atom-centered polarizabilities, and also nonelectrostatic repulsion, all calculated at the B3LYP/cc-pVDZ level of theory. The resulting excitation energies and solvent shifts are shown in Table 3. For

Table 3. Excitation Energy and Solvent Shift of MnO_4^- in Water Solvent: Convergence with Respect to Core Region Size

$R_c^{a,b}$ (Å)	$E_{\text{exc}}^{\text{sol}}$ (eV)		ΔE_{exc} (eV)	
	PE	PDE	PE	PDE
0.0 (0.0)	2.002	2.074	0.046	0.118
2.0 (3.1)	2.024	2.061	0.068	0.106
2.4 (6.8)	2.038	2.053	0.082	0.097
2.8 (9.5)	2.043	2.051	0.087	0.095
3.2 (13.2)	2.046	2.050	0.090	0.094

^aCore-region cutoff value defined as the minimum distance between any atom in the solute and a solvent molecule. ^bAverage number of core-region water molecules are given in parentheses.

comparison, we also include results of the basic PE model where we used atom-centered multipole moments up to quadrupoles and polarizabilities also calculated using B3LYP/cc-pVDZ. The solvent shift is calculated by subtracting the vacuum excitation energy from the excitation energy of the solvated system ($\Delta E_{\text{exc}} = E_{\text{exc}}^{\text{sol}} - E_{\text{exc}}^{\text{vac}}$).

The calculated vacuum excitation energy ($E_{\text{exc}}^{\text{vac}}$) is 1.956 eV, in good agreement with the experimental value of 2.19 eV.⁸³ The excitation energy obtained using the PDE model including only MnO_4^- in the core region is 2.074 eV. This is only 0.024 eV higher than the value of 2.050 eV obtained when convergence in the size of the core region is obtained, and we thus see that the PDE model performs very well already when including only MnO_4^- in the core region. This is an improvement compared to the PE model, which gives rise to changes in the excitation energy of 0.044 eV when including the same number of water molecules in the core region. However, the gain in performance when using the PDE model is in fact minor as compared to the PE model, and this comparison therefore also confirms the usually good performance of the basic PE model.

The experimentally determined solvent shift for this excitation energy is 0.10 ± 0.01 eV,⁸³ in very good agreement with the predictions of the PDE model. Including water molecules in the core region, the shift in the excitation energy changes from 0.118 to 0.094 eV and is thus rather insensitive to whether water molecules are included in the core region or not. The good agreement with experiment is partly due to the fact that vibrational effects are, to a certain degree, included in the

structures via the MD simulation, and also because of the advanced description of the solvent effects. Continuum solvation models seem less successful in capturing this solvent shift: a blueshift of 0.013 eV is obtained when calculating the excitation energies at the (PCM-)CAM-B3LYP/cc-pVDZ// (PCM-)BLYP/6-31G level of theory, clearly underestimating the experimental observations.

In order to evaluate the effect of the new components of the embedding potential, i.e., the improved electrostatics and the nonelectrostatic repulsion, we also performed calculations using the PDE model without nonelectrostatic repulsion (PDE-R) and using the PE model with nonelectrostatic repulsion (PE+R), as well as calculations with scaled nonelectrostatic repulsion (indicated by *). The results are presented in Table 4. Note that the effect of the individual contributions

Table 4. Excitation Energy and Solvent Shift of MnO_4^- in Water Solvent: Embedding Potential Analysis

model ^a	$E_{\text{exc}}^{\text{sol}}$ (eV)	ΔE_{exc} (eV)
PE	2.002	0.046
PDE	2.074	0.118
PDE-R	1.971	0.015
PE+R	2.077	0.121
PDE*	2.059	0.104
PE+R*	2.070	0.114

^aCore region consists of MnO_4^- , all water molecules are described by the indicated embedding potential. *Nonelectrostatic repulsion was scaled by a factor of 0.8.

(e.g., electrostatics or induction) is not directly comparable between two calculations that employ different embedding potentials, since it depends on the wave function/density of the core region. Removing or altering one part of the embedding potential will affect all the contributions. Nonetheless, it is evident that the nonelectrostatic repulsion is essential in order to obtain good agreement with the experimental solvent shift. The effect of the nonelectrostatic repulsion on the shift obtained using an explicit density description of the electrostatics is 0.103 eV, as shown by a comparison between PDE and PDE-R. This is slightly higher than its effect when using a multipole moment description where the shift is increased by 0.075 eV. This indicates that the good performance that is often obtained using the PE model is due to the weaker electrostatic interactions that mimic the effect of nonelectrostatic repulsion. This is consistent with the interaction energy analysis presented in the previous subsection. The interaction energy analysis also revealed that the repulsive effect is too strong which partly accounts for the overestimated shift obtained using the PDE model with the smallest core region. Good agreement was obtained when the nonelectrostatic repulsion was scaled by a factor of 0.8, and this is also confirmed here where a shift of 0.104 eV is obtained, which is closer to the converged shift of 0.094 eV.

In the calculations discussed above, we only used a core region and either an inner region or an outer region. An interesting aspect of the PDE model is the possibility to use a three-layered model where only a limited number of fragments are included in the inner region, since these can be computationally more expensive than outer-region fragments, while all other fragments are placed in the outer region. In Table 5, we show results of calculations on a single structure (randomly chosen), where the number of fragments in the

Table 5. Excitation Energy of MnO_4^- in Water Solvent: Convergence with Respect to Inner Region Size

$R_{\text{in}}^{a,b}$ (Å)	$E_{\text{exc}}^{\text{sol}}$ (eV)
	PDE
2.0 (3)	2.088
3.0 (12)	2.119
4.0 (25)	2.123
5.0 (41)	2.123

^aInner-region cutoff value defined as the minimum distance between any atom in the solute and a solvent molecule. ^bNumber of inner-region water molecules are given in parentheses (all remaining water molecules are in the outer region).

inner region is gradually increased. We find that the excitation energy converges quickly, as might be expected because we already know that the classical embedding potentials accurately reproduce the molecular electrostatic potential, especially at longer distances.^{25,34}

***p*-Nitroaniline.** Next we apply the PDE model to *p*-nitroaniline (pNA) in water and compare the performance of the PDE model to the PE model. We calculate the energy of the lowest singlet $\pi \rightarrow \pi^*$ charge-transfer transition. Experimentally, a large redshift of about -0.98 eV is observed between pNA in gas phase⁸⁴ (4.24 eV) and water solution⁸⁵ (3.26 eV). The structures used were taken from a rigid body classical MD simulation⁷⁸ and therefore include solvent dynamics but not vibrational effects. We applied a spherical cutoff distance from pNA of 10.0 Å, which amounts to 268 water molecules on average, averaged over 120 structures. The results from our calculations are presented in Table 6 together

Table 6. Excitation Energy and Solvent Shift of pNA in Water Solution: Convergence with Respect to Core Region Size

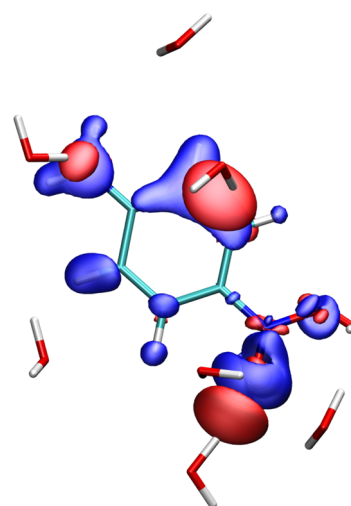
$R_{\text{c}}^{a,b}$ (Å)	$E_{\text{exc}}^{\text{sol}}$ (eV)		ΔE_{exc} (eV)	
	PE	PDE	PE	PDE
0.0 (0.0)	3.642	3.769	-0.726	-0.600
2.0 (1.3)	3.659	3.748	-0.710	-0.621
2.2 (2.4)	3.665	3.738	-0.703	-0.630
2.4 (4.1)	3.667	3.731	-0.701	-0.637
2.6 (6.8)	3.669	3.723	-0.699	-0.646
3.0 (14.4)	3.670	3.707	-0.698	-0.662
4.0 (31.9)	3.668	3.681	-0.701	-0.688

^aCore-region cutoff value defined as the minimum distance between any atom in the solute and a solvent molecule. ^bAverage number of core-region water molecules are given in parentheses.

with conventional PE results. Both the PDE and PE results are obtained at the CAM-B3LYP/6-31+G* level of theory, using an embedding potential based on B3LYP/6-31+G* calculations. The 6-31+G* basis set was chosen based on a basis set analysis performed on a random snapshot (see Table S2 in the Supporting Information). The vacuum excitation energy is 4.368 eV calculated at the CAM-B3LYP/6-31+G**/B3LYP/aug-cc-pVTZ level of theory (the pNA structure used in the MD simulation is based on a PCM-B3LYP/aug-cc-pVTZ optimized structure).

The difference between the PDE- and PE-based solvent shifts is 0.126 eV when no water molecules are included in the core region. This is larger than the difference observed for MnO_4^- (0.072 eV). Interestingly, in this case, it is the PE model that is

closest to the converged value for the excitation energy (i.e., the observed changes when increasing the number of water molecules in the core region is less for PE than for PDE). With no water molecules in the core region, the PDE model overshoots by ~ 0.10 eV compared to only ~ 0.03 eV by the PE model. This difference in behavior compared to MnO_4^- can partly be explained by the overestimated nonelectrostatic repulsion that we observed in the interaction energy analysis, where we also found that the use of larger basis sets leads to an additional increase of nonelectrostatic repulsion. This is confirmed by the fact that scaling the repulsion by a factor of 0.8 leads to a lowering of the excitation energy from 3.769 to 3.746 eV. However, we note that the lack of nonelectrostatic repulsion in the PE model is likely to lead to artificial stabilization of the wave function/density because it is allowed to penetrate too deeply into the environment. This effect can be seen by plotting the density difference between the PE and PDE models as shown in Figure 3. Here we see that the PE

**Figure 3.** Electron density difference between PE and PDE of a pNA-water cluster (isovalues: red = 0.001, blue = -0.001). Only the pNA is in the core region, while the water molecules are either in the inner region or in the outer region.

model results in higher electron density close to the water molecules (shown in red) and depleted electron density close to the nuclei (shown in blue) compared to the PDE model. It is likely that this effect mimics charge-transfer effects that are present in a full quantum-mechanical treatment (as demonstrated in Figure 4). This makes it difficult to compare the excitation energies obtained when increasing the size of the core region, since the delocalization into the environment increases at the same time. Both the PE and PDE models are off by approximately 0.3–0.4 eV in their predictions of the solvent shifts compared to experimental data, a failure that has been shown to be related to the TD-DFT formalism.⁸⁶ It is therefore difficult to draw decisive conclusions concerning the relative merits of the two approaches in this case.

The nonelectrostatic repulsion enforces orthogonality between fragments in the core region and the inner region. However, the fragments in the inner or outer regions are not orthogonalized internally. This is a good approximation when the fragments are well-separated in space, but it is not clear what the effect is for close-lying fragments. Certainly, they are not as severe as the nonorthogonality approximation between

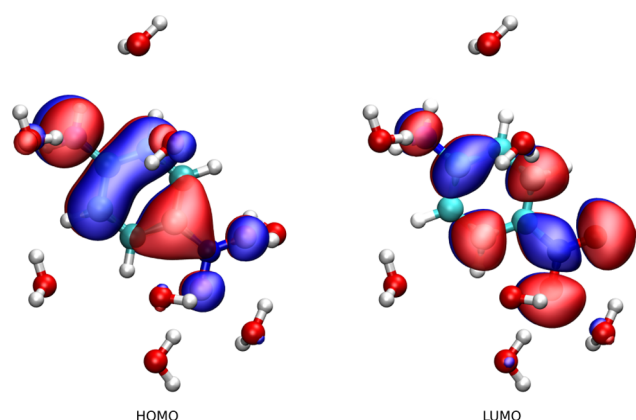


Figure 4. Highest occupied (a) and lowest unoccupied (b) molecular orbitals of a pNA-water cluster calculated at CAM-B3LYP/6-31+G* level of theory.

core- and inner-/outer-region fragments because the densities are optimized in isolation, thus avoiding potential “electron-spill” effects. This approximation can affect the properties of the core region through the electrostatic interactions and secondarily via altered polarization. We have performed additional excitation energy calculations on a geometry-optimized pNA–water trimer to get an estimate of the effect (see Table 7). The system was designed so that both water

Table 7. Excitation Energies in Geometry-Optimized pNA–Water Dimers/Trimer

system ^b	QM	E_{exc} (eV)		ΔE_{exc} ^a (eV)	
		PE	PDE	PE	PDE
pNA + H ₂ O ^c	4.142	4.138	4.160	−0.004	0.018
pNA + H ₂ O ^d	4.147	4.145	4.156	−0.002	0.009
pNA + 2H ₂ O	4.045	4.039	4.071	−0.006	0.026

^aDifference compared to QM. ^bGeometry is shown in Figure 5. ^cWater molecule no. 1 (see Figure 5). ^dWater molecule no. 2 (see Figure 5).

molecules hydrogen bond to pNA and to each other simultaneously, so as to get the largest possible effect while still retaining a reasonable structure (see Figure 5). The pNA is always placed in the core region while the water molecules are either in the core region (QM), in the inner region (PDE), or in the outer region (PE). By comparing the error of the PDE and PE models relative to a full quantum-mechanical treatment, we observe that the error is cumulative, which suggests that the

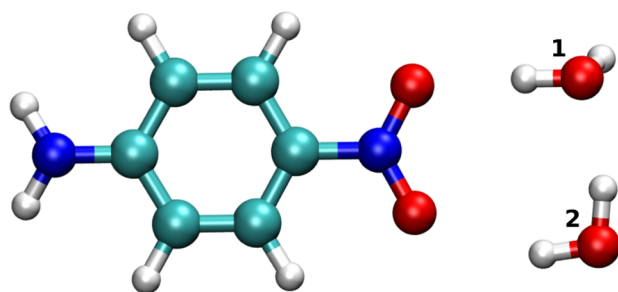


Figure 5. Geometry-optimized structure of pNA and two water molecules (B3LYP/6-31+G*). The water molecule enumeration is used in Table 7.

error from using nonorthogonalized fragment densities is negligible.

SUMMARY AND OUTLOOK

In this paper, we have presented the theory and implementation of a new QM/QM/MM-based method termed the polarizable density embedding (PDE) model. The model allows for a layered description of the environment, reflected in the derived embedding potential. Furthermore, the method is fully polarizable in a self-consistent way in both the core region and the environment. The implementation of the method is flexible and allows for both ground- and excited-state calculations. Sample calculations have been presented for dimer interaction energies as well as for excitation energies of two solvated chromophores. The PDE model shows promising results but further validation, especially in relation to the nonelectrostatic repulsion part of the embedding potential, needs to be explored. The implementation of the PDE model presented here has been limited to Hartree–Fock (HF) and Kohn–Sham density functional theory (KS-DFT). However, the method itself is not limited to the use of these approaches for the core region, and the extension of the approach to other quantum-chemical methods such as multiconfigurational self-consistent field (MCSCF) and coupled-cluster (CC) theory will be implemented in the near future. Our sample calculations have only considered systems consisting of noncovalently bonded fragments (molecules). The extension of the PDE model to the case of more complex systems such as proteins is currently being formulated.

ASSOCIATED CONTENT

Supporting Information

Basis set convergence of the excitation energies and solvent shifts of MnO₄[−] and pNA in vacuum and in water solvent. This material is available free of charge via the Internet at <http://pubs.acs.org>.

AUTHOR INFORMATION

Corresponding Authors

*E-mail: magnus.olsen@epfl.ch.

*E-mail: kongsted@sdu.dk.

Notes

The authors declare no competing financial interest.

ACKNOWLEDGMENTS

J.M.H.O. acknowledges financial support from the research career program Sapere Aude of the Danish Council for Independent Research (DFR). J.K. thanks the Danish Council for Independent Research (the Sapere Aude program), the Villum Foundation, the Lundbeck Foundation, and the Danish e-Infrastructure Cooperation (DeIC) for financial support. K.R. has received support from the European Research Council through a Starting Grant (Grant 279619) and the Research Council of Norway through a Centre of Excellence Grant (Grant 179568).

REFERENCES

- (1) Tomasi, J.; Mennucci, B.; Cammi, R. Quantum Mechanical Continuum Solvation Models. *Chem. Rev.* **2005**, *105*, 2999–3094.
- (2) Gordon, M. S.; Fedorov, D. G.; Pruitt, S. R.; Slipchenko, L. V. Fragmentation Methods: A Route to Accurate Calculations on Large Systems. *Chem. Rev.* **2012**, *112*, 632–672.

- (3) Miertus, S.; Scrocco, E.; Tomasi, J. Electrostatic Interaction of a Solute with a Continuum. A Direct Utilization of AB Initio Molecular Potentials for the Prediction of Solvent Effects. *Chem. Phys.* **1981**, *55*, 117–129.
- (4) Miertus, S.; Tomasi, J. Approximate Evaluations of the Electrostatic Free Energy and Internal Energy Changes in Solution Processes. *Chem. Phys.* **1982**, *65*, 239–245.
- (5) Cancès, E.; Mennucci, B.; Tomasi, J. A New Integral Equation Formalism for the Polarizable Continuum Model: Theoretical Background and Applications to Isotropic and Anisotropic Dielectrics. *J. Chem. Phys.* **1997**, *107*, 3032.
- (6) Warshel, A.; Levitt, M. Theoretical Studies of Enzymic Reactions: Dielectric, Electrostatic and Steric Stabilization of the Carbonium Ion in the Reaction of Lysozyme. *J. Mol. Biol.* **1976**, *103*, 227–249.
- (7) Lin, H.; Truhlar, D. QM/MM: What Have We Learned, Where Are We, and Where Do We Go From Here? *Theor. Chem. Acc.* **2007**, *117*, 185–199.
- (8) Senn, H. M.; Thiel, W. QM/MM Methods for Biomolecular Systems. *Angew. Chem., Int. Ed.* **2009**, *48*, 1198–1229.
- (9) Xu, Z.; Matsika, S. Combined Multireference Configuration Interaction/ Molecular Dynamics Approach for Calculating Solvatochromic Shifts: Application to the $n_{\text{O}} \rightarrow \pi^*$ Electronic Transition of Formaldehyde. *J. Phys. Chem. A* **2006**, *110*, 12035–12043.
- (10) Kistler, K. A.; Matsika, S. Solvatochromic Shifts of Uracil and Cytosine Using a Combined Multireference Configuration Interaction/Molecular Dynamics Approach and the Fragment Molecular Orbital Method. *J. Phys. Chem. A* **2009**, *113*, 12396–12403.
- (11) Fox, S. J.; Pittcock, C.; Fox, T.; Tautermann, C. S.; Malcolm, N.; Skylaris, C.-K. Electrostatic Embedding in Large-Scale First Principles Quantum Mechanical Calculations on Biomolecules. *J. Chem. Phys.* **2011**, *135*, 224107.
- (12) Wang, B.; Truhlar, D. G. Partial Atomic Charges and Screened Charge Models of the Electrostatic Potential. *J. Chem. Theory Comput.* **2012**, *8*, 1989–1998.
- (13) Day, P.; Jensen, J.; Gordon, M.; Webb, S.; Stevens, W.; Krauss, M.; Garmer, D.; Basch, H.; Cohen, D. An Effective Fragment Method for Modeling Solvent Effects in Quantum Mechanical Calculations. *J. Chem. Phys.* **1996**, *105*, 1968–1986.
- (14) Gordon, M.; Freitag, M.; Bandyopadhyay, P.; Jensen, J.; Kairys, V.; Stevens, W. The Effective Fragment Potential Method: A QM-Based MM Approach to Modeling Environmental Effects in Chemistry. *J. Phys. Chem. A* **2001**, *105*, 293–307.
- (15) Jensen, L.; van Duijnen, P. T.; Snijders, J. G. A Discrete Solvent Reaction Field Model within Density Functional Theory. *J. Chem. Phys.* **2003**, *118*, 514–521.
- (16) Kongsted, J.; Østed, A.; Mikkelsen, K. V.; Christiansen, O. Coupled Cluster/Molecular Mechanics Method: Implementation and Application to Liquid Water. *J. Phys. Chem. A* **2003**, *107*, 2578–2588.
- (17) Nielsen, C. B.; Christiansen, O.; Mikkelsen, K. V.; Kongsted, J. Density Functional Self-Consistent Quantum Mechanics/Molecular Mechanics Theory for Linear and Nonlinear Molecular Properties: Applications to Solvated Water and Formaldehyde. *J. Chem. Phys.* **2007**, *126*, 154112.
- (18) Curutchet, C.; Muñoz-Losa, A.; Monti, S.; Kongsted, J.; Scholes, G. D.; Mennucci, B. Electronic Energy Transfer in Condensed Phase Studied by a Polarizable QM/MM Model. *J. Chem. Theory Comput.* **2009**, *5*, 1838–1848.
- (19) Boulanger, E.; Thiel, W. Toward QM/MM Simulation of Enzymatic Reactions with the Drude Oscillator Polarizable Force Field. *J. Chem. Theory Comput.* **2014**, *10*, 1795–1809.
- (20) Caprasecca, S.; Jurinovich, S.; Viani, L.; Curutchet, C.; Mennucci, B. Geometry Optimization in Polarizable QM/MM Models: The Induced Dipole Formulation. *J. Chem. Theory Comput.* **2014**, *10*, 1588–1598.
- (21) Steindal, A. H.; Ruud, K.; Frediani, L.; Aidas, K.; Kongsted, J. Excitation Energies in Solution: The Fully Polarizable QM/MM/PCM Method. *J. Phys. Chem. B* **2011**, *115*, 3027–3037.
- (22) Caprasecca, S.; Curutchet, C.; Mennucci, B. Toward a Unified Modeling of Environment and Bridge-Mediated Contributions to Electronic Energy Transfer: A Fully Polarizable QM/MM/PCM Approach. *J. Chem. Theory Comput.* **2012**, *8*, 4462–4473.
- (23) Jurinovich, S.; Pescitelli, G.; Di Bari, L.; Mennucci, B. A TDDFT/MMPol/PCM Model for the Simulation of Exciton-Coupled Circular Dichroism Spectra. *Phys. Chem. Chem. Phys.* **2014**, *16*, 16407–16418.
- (24) Lipparini, F.; Barone, V. Polarizable Force Fields and Polarizable Continuum Model: A Fluctuating Charges/PCM Approach. 1. Theory and Implementation. *J. Chem. Theory Comput.* **2011**, *7*, 3711–3724.
- (25) Olsen, J. M.; Aidas, K.; Kongsted, J. Excited States in Solution through Polarizable Embedding. *J. Chem. Theory Comput.* **2010**, *6*, 3721–3734.
- (26) Olsen, J. M. H.; Kongsted, J. Molecular Properties through Polarizable Embedding. *Adv. Quantum Chem.* **2011**, *61*, 107–143.
- (27) Sneskov, K.; Schwabe, T.; Kongsted, J.; Christiansen, O. The Polarizable Embedding Coupled Cluster Method. *J. Chem. Phys.* **2011**, *134*, 104108.
- (28) Schwabe, T.; Sneskov, K.; Olsen, J. M. H.; Kongsted, J.; Christiansen, O.; Hättig, C. PERI-CC2: A Polarizable Embedded RI-CC2 Method. *J. Chem. Theory Comput.* **2012**, *8*, 3274–3283.
- (29) Hedegård, E. D.; List, N. H.; Jensen, H. J. Aa.; Kongsted, J. The Multi-Configuration Self-Consistent Field Method Within a Polarizable Embedded Framework. *J. Chem. Phys.* **2013**, *139*, 044101.
- (30) Pedersen, M. N.; Hedegård, E. D.; Olsen, J. M. H.; Kauczor, J.; Norman, P.; Kongsted, J. Damped Response Theory in Combination with Polarizable Environments: The Polarizable Embedding Complex Polarization Propagator Method. *J. Chem. Theory Comput.* **2014**, *10*, 1164–1171.
- (31) Steinmann, C.; Olsen, J. M. H.; Kongsted, J. Nuclear Magnetic Shielding Constants From Quantum Mechanical/Molecular Mechanical Calculations Using Polarizable Embedding: Role of the Embedding Potential. *J. Chem. Theory Comput.* **2014**, *10*, 981–988.
- (32) Olsen, J.; Jørgensen, P. Linear and Non-Linear Response Functions for an Exact State and for an MCSCF State. *J. Chem. Phys.* **1985**, *82*, 3235–3264.
- (33) Helgaker, T.; Coriani, S.; Jørgensen, P.; Kristensen, K.; Olsen, J.; Ruud, K. Recent Advances in Wave Function-Based Methods of Molecular-Property Calculations. *Chem. Rev.* **2012**, *112*, 543–631.
- (34) Schwabe, T.; Olsen, J. M. H.; Sneskov, K.; Kongsted, J.; Christiansen, O. Solvation Effects on Electronic Transitions: Exploring the Performance of Advanced Solvent Potentials in Polarizable Embedding Calculations. *J. Chem. Theory Comput.* **2011**, *7*, 2209–2217.
- (35) Huzinaga, S.; Cantu, A. A. Theory of Separability of Many-Electron Systems. *J. Chem. Phys.* **1971**, *55*, 5543–5549.
- (36) Kitaura, K.; Ikeo, E.; Asada, T.; Nakano, T.; Uebayasi, M. Fragment Molecular Orbital Method: An Approximate Computational Method for Large Molecules. *Chem. Phys. Lett.* **1999**, *313*, 701–706.
- (37) Fedorov, D. G.; Kitaura, K. Extending the Power of Quantum Chemistry to Large Systems with the Fragment Molecular Orbital Method. *J. Phys. Chem. A* **2007**, *111*, 6904–6914.
- (38) Wesolowski, T. A.; Warshel, A. Frozen Density Functional Approach for Ab Initio Calculations of Solvated Molecules. *J. Phys. Chem.* **1993**, *97*, 8050–8053.
- (39) Wesolowski, T.; Weber, J. Kohn-Sham Equations with Constrained Electron Density: An Iterative Evaluation of the Ground-State Electron Density of Interacting Molecules. *Chem. Phys. Lett.* **1996**, *248*, 71–76.
- (40) Jacob, C. R.; Neugebauer, J.; Visscher, L. A Flexible Implementation of Frozen-Density Embedding for use in Multilevel Simulations. *J. Comput. Chem.* **2008**, *29*, 1011–1018.
- (41) Neugebauer, J. On the Calculation of General Response Properties in Subsystem Density Functional Theory. *J. Chem. Phys.* **2009**, *131*, 084104.
- (42) Höfener, S.; Severo Pereira Gomes, A.; Visscher, L. Molecular Properties via a Subsystem Density Functional Theory Formulation: A Common Framework for Electronic Embedding. *J. Chem. Phys.* **2012**, *136*, 044104.

- (43) Piquemal, J.-P.; Cisneros, G. A.; Reinhardt, P.; Gresh, N.; Darden, T. A. Towards a Force Field Based on Density Fitting. *J. Chem. Phys.* **2006**, *124*, 104101.
- (44) Cisneros, G. A.; Piquemal, J.-P.; Darden, T. A. Quantum Mechanics/Molecular Mechanics Electrostatic Embedding with Continuous and Discrete Functions. *J. Phys. Chem. B* **2006**, *110*, 13682–13684.
- (45) Barandiarán, Z.; Seijo, L. The Ab Initio Model Potential Representation of the Crystalline Environment. Theoretical Study of the Local Distortion on NaCl:Cu⁺. *J. Chem. Phys.* **1988**, *89*, 5739–5746.
- (46) Swerts, B.; Chibotaru, L. F.; Lindh, R.; Seijo, L.; Barandiarán, Z.; Clima, S.; Pierloot, K.; Hendrickx, M. F. A. Embedding Fragment Ab Initio Model Potentials in CASSCF/CASPT2 Calculations of Doped Solids: Implementation and Applications. *J. Chem. Theory Comput.* **2008**, *4*, 586–594.
- (47) Daday, C.; König, C.; Valsson, O.; Neugebauer, J.; Filippi, C. State-Specific Embedding Potentials for Excitation-Energy Calculations. *J. Chem. Theory Comput.* **2013**, *9*, 2355–2367.
- (48) Olsen, J. M. H. Development of Quantum Chemical Methods Towards Rationalization and Optimal Design of Photoactive Proteins. Ph.D. Thesis, University of Southern Denmark, Odense, Denmark, 2012; DOI: 10.6084/m9.figshare.156852.
- (49) Stone, A. J. The Induction Energy of an Assembly of Polarizable Molecules. *Chem. Phys. Lett.* **1989**, *155*, 102–110.
- (50) Surján, P.; Ángyán, J. G. The Reliability of the Point Charge Model Representing Intermolecular Effects in Ab Initio Calculations. *Chem. Phys. Lett.* **1994**, *225*, 258–264.
- (51) Fradelos, G.; Wesolowski, T. A. Importance of the Intermolecular Pauli Repulsion in Embedding Calculations for Molecular Properties: The Case of Excitation Energies for a Chromophore in Hydrogen-Bonded Environments. *J. Phys. Chem. A* **2011**, *115*, 10018–10026.
- (52) Aidas, K.; Angeli, C.; Bak, K. L.; Bakken, V.; Bast, R.; Boman, L.; Christiansen, O.; Cimiraglia, R.; Coriani, S.; Dahle, P.; et al. The Dalton Quantum Chemistry Program System. *Wiley Interdiscip. Rev.: Comput. Mol. Sci.* **2014**, *4*, 269–284.
- (53) Gagliardi, L.; Lindh, R.; Karlström, G. Local Properties of Quantum Chemical Systems: The LoProp Approach. *J. Chem. Phys.* **2004**, *121*, 4494–4500.
- (54) Aquilante, F.; De Vico, L.; Ferré, N.; Ghigo, G.; Malmqvist, P.-A.; Neogrády, P.; Pedersen, T. B.; Pitoňák, M.; Reiher, M.; Roos, B. O.; et al. MOLCAS 7: The Next Generation. *J. Comput. Chem.* **2010**, *31*, 224–247.
- (55) Frisch, M. J.; Trucks, G. W.; Schlegel, H. B.; Scuseria, G. E.; Robb, M. A.; Cheeseman, J. R.; Scalmani, G.; Barone, V.; Mennucci, B.; Petersson, G. A. et al. *Gaussian 09*, revision A.02; Gaussian, Inc., Wallingford, CT, 2009.
- (56) Olsen, J. M. H. *PELib: The Polarizable Embedding Library (Development Version)*, 2014.
- (57) Gao, B. *Gen1Int*, version 0.2.1; 2014.
- (58) Gao, B.; Thorvaldsen, A. J.; Ruud, K. GEN1INT: A Unified Procedure for the Evaluation of One-Electron Integrals over Gaussian Basis Functions and Their Geometric Derivatives. *Int. J. Quantum Chem.* **2011**, *111*, 858–872.
- (59) Becke, A. D. Density-Functional Exchange-Energy Approximation with Correct Asymptotic Behavior. *Phys. Rev. A* **1988**, *38*, 3098–3100.
- (60) Lee, C.; Yang, W.; Parr, R. G. Development of the Colle-Salvetti Correlation-Energy Formula into a Functional of the Electron Density. *Phys. Rev. B* **1988**, *37*, 785–789.
- (61) Miehlich, B.; Savin, A.; Stoll, H.; Preuss, H. Results Obtained with the Correlation Energy Density Functionals of Becke and Lee, Yang and Parr. *Chem. Phys. Lett.* **1989**, *157*, 200–206.
- (62) Becke, A. D. Density-Functional Thermochemistry. III. The Role of Exact Exchange. *J. Chem. Phys.* **1993**, *98*, 5648–5652.
- (63) Vosko, S. H.; Wilk, L.; Nusair, M. Accurate Spin-Dependent Electron Liquid Correlation Energies for Local Spin Density Calculations: A Critical Analysis. *Can. J. Phys.* **1980**, *58*, 1200–1211.
- (64) Stephens, P. J.; Devlin, F. J.; Chabalowski, C. F.; Frisch, M. J. Ab Initio Calculation of Vibrational Absorption and Circular Dichroism Spectra Using Density Functional Force Fields. *J. Phys. Chem.* **1994**, *98*, 11623–11627.
- (65) Yanai, T.; Tew, D. P.; Handy, N. C. A New Hybrid Exchange–Correlation Functional Using the Coulomb-Attenuating Method (CAM-B3LYP). *Chem. Phys. Lett.* **2004**, *393*, 51–57.
- (66) Hehre, W. J.; Ditchfield, R.; Pople, J. A. Self-Consistent Molecular Orbital Methods. XII. Further Extensions of Gaussian-Type Basis Sets for Use in Molecular Orbital Studies of Organic Molecules. *J. Chem. Phys.* **1972**, *56*, 2257–2261.
- (67) Hariharan, P.; Pople, J. The Influence of Polarization Functions on Molecular Orbital Hydrogenation Energies. *Theor. Chim. Acta* **1973**, *28*, 213–222.
- (68) Franci, M. M.; Pietro, W. J.; Hehre, W. J.; Binkley, J. S.; Gordon, M. S.; DeFrees, D. J.; Pople, J. A. Self-Consistent Molecular Orbital Methods. XXIII. A Polarization-Type Basis Set for Second-Row Elements. *J. Chem. Phys.* **1982**, *77*, 3654–3665.
- (69) Clark, T.; Chandrasekhar, J.; Spitznagel, G. W.; Schleyer, P. V. R. Efficient Diffuse Function-Augmented Basis Sets for Anion Calculations. III. The 3-21+G Basis Set for First-Row Elements, LiF. *J. Comput. Chem.* **1983**, *4*, 294–301.
- (70) Dunning, T. H. Gaussian Basis Sets for Use in Correlated Molecular Calculations. I. The Atoms Boron Through Neon and Hydrogen. *J. Chem. Phys.* **1989**, *90*, 1007–1023.
- (71) Kendall, R. A.; Dunning, T. H.; Harrison, R. J. Electron Affinities of the First-Row Atoms Revisited. Systematic Basis Sets and Wave Functions. *J. Chem. Phys.* **1992**, *96*, 6796–6806.
- (72) Woon, D. E.; Dunning, T. H. Gaussian Basis Sets for Use in Correlated Molecular Calculations. III. The Atoms Aluminum Through Argon. *J. Chem. Phys.* **1993**, *98*, 1358–1371.
- (73) Balabanov, N. B.; Peterson, K. A. Systematically Convergent Basis Sets for Transition Metals. I. All-Electron Correlation Consistent Basis Sets for the 3d Elements Sc–Zn. *J. Chem. Phys.* **2005**, *123*, 064107.
- (74) Jorgensen, W. L.; Chandrasekhar, J.; Madura, J. D.; Impey, R. W.; Klein, M. L. Comparison of Simple Potential Functions for Simulating Liquid Water. *J. Chem. Phys.* **1983**, *79*, 926–935.
- (75) Hehre, W. J.; Stewart, R. F.; Pople, J. A. Self-Consistent Molecular-Orbital Methods. I. Use of Gaussian Expansions of Slater-Type Atomic Orbitals. *J. Chem. Phys.* **1969**, *51*, 2657–2664.
- (76) Pietro, W. J.; Hehre, W. J. Molecular Orbital Theory of the Properties of Inorganic and Organometallic Compounds. 3. STO-3G Basis Sets for First- and Second-Row Transition Metals. *J. Comput. Chem.* **1983**, *4*, 241–251.
- (77) Ufimtsev, I.; Martinez, T. Quantum Chemistry on Graphical Processing Units. 3. Analytical Energy Gradients and First Principles Molecular Dynamics. *J. Chem. Theory Comput.* **2009**, *5*, 2619.
- (78) Snegov, K.; Schwabe, T.; Christiansen, O.; Kongsted, J. Scrutinizing the Effects of Polarization in QM/MM Excited State Calculations. *Phys. Chem. Chem. Phys.* **2011**, *13*, 18551–18560.
- (79) Boys, S.; Bernardi, F. The Calculation of Small Molecular Interactions by the Differences of Separate Total Energies. Some Procedures with Reduced Errors. *Mol. Phys.* **1970**, *19*, 553–566.
- (80) van Duijneveldt, F. B.; van Duijneveldt-van de Rijdt, J. G. C. M.; van Lenthe, J. H. State of the Art in Counterpoise Theory. *Chem. Rev.* **1994**, *94*, 1873–1885.
- (81) Söderhjelm, P.; Karlström, G.; Ryde, U. Comparison of Overlap-Based Models for Approximating the Exchange-Repulsion Energy. *J. Chem. Phys.* **2006**, *124*, 244101.
- (82) Söderhjelm, P.; Öhrn, A. On the Coupling of Intermolecular Polarization and Repulsion Through Pseudo-Potentials. *Chem. Phys. Lett.* **2009**, *468*, 94–99.
- (83) Houmøller, J.; Kaufman, S. H.; Stöckel, K.; Tribedi, L. C.; Brøndsted Nielsen, S.; Weber, J. M. On the Photoabsorption by Permanganate Ions in Vacuo and the Role of a Single Water Molecule. New Experimental Benchmarks for Electronic Structure Theory. *ChemPhysChem* **2013**, *14*, 1133–1137.

- (84) Millefiori, S.; Favini, G.; Millefiori, A.; Grasso, D. Electronic Spectra and Structure of Nitroanilines. *Spectrochim. Acta, Part A* **1977**, *33*, 21–27.
- (85) Thomsen, C. L.; Thøgersen, J.; Keiding, S. R. Ultrafast Charge-Transfer Dynamics: Studies of *p*-Nitroaniline in Water and Dioxane. *J. Phys. Chem. A* **1998**, *102*, 1062–1067.
- (86) Eriksen, J. J.; Sauer, S. P.; Mikkelsen, K. V.; Christiansen, O.; Jensen, H. J. A.; Kongsted, J. Failures of TDDFT in Describing the Lowest Intramolecular Charge-Transfer Excitation in para-Nitroaniline. *Mol. Phys.* **2013**, *111*, 1235–1248.